LINEAR PARAMETER-VARYING GAIN-SCHEDULED ATTITUDE CONTROLLER FOR AN ON-ORBIT SERVICING MISSION INVOLVING FLEXIBLE LARGE SPACECRAFT AND FUEL SLOSHING

Ricardo Rodrigues(1), **Francesco Sanfedino**(1), **Daniel Alazard**(1), **Valentin Preda**(2), **Javier Olucha**(3)

(1)*Institut Supérieur de l'Aéronautique et de l'Espace (ISAE-SUPAERO), Université de Toulouse, 10 Avenue Edouard Belin, BP-54032, 31055, Toulouse Cedex 4, France, ricardo.rodrigues@isae-supaero.fr, francesco.sanfedino@isae-supaero.fr, daniel.alazard@isae-supaero.fr*
(2)*European Space Agency (GNC, AOCS & Pointing Division), ESTEC, Noordwijk, the Netherlands, valentin.preda@esa.int*
(3)*Department of Electrical Engineering, Eindhoven University of Technology, P.O. Box 513, 5600 MB Eindhoven, the Netherlands, e.j.olucha.delgado@student.tue.nl*

ABSTRACT

In this paper, a comprehensive methodology is presented for modeling an on-orbit servicing (OOS) mission scenario and designing a gain-scheduled feedback control system that can robustly meet performance requirements. This methodology accounts for uncertainties in the model, as well as significant changes in inertia and flexibility throughout the mission scenario. To capture the dynamics and interactions of all subsystems in the OOS scenario, a single linear fractional representation (LFR) was developed for the uncertain plant, taking into account the varying geometrical configuration of a robotic arm, flexible appendages and sloshing dynamics. The controller design considers the interactions between subsystems and uncertainties, as well as the time-varying and coupled flexible dynamics. Finally, the paper evaluates the robust stability and worst-case performances of the closed-loop system using a structured singular value analysis.

1 INTRODUCTION

On-orbit servicing (OOS) technology refers to the use of spacecraft or robots to service, repair or upgrade satellites while they are still in orbit. This technology has the potential to extend the lifespan of satellites by allowing them to be serviced and repaired instead of being immediately replaced once they malfunction or run out of fuel [1]. However, this technology is complex and challenging in many ways. Numerous studies have investigated the issue of spacecraft rendezvous and assembly with disturbance rejection, using various strategies. Liu *et al.* [2] developed a sampled-data approach to optimize actions against disturbance and limited measurements in a rendezvous problem between two spacecraft, while other researchers proposed controls such as adaptive active disturbance rejection control and higher-order sliding mode control to address uncertainty in disturbance torques during spacecraft rendezvous [3, 4]. Some studies have presented a Guidance, Navigation and Control (GNC) framework for rendezvous/docking [5], while Chai *et al.* [6] introduced a robust attitude control for on-orbit assembly to manage the attitude of a substructure under disturbance. However, most of these studies have assumed the system to be a rigid body, disregarding any potential flexibility. Rodrigues *et al.* [7] proposed a comprehensive approach for modeling an on-orbit servicing mission scenario. Nevertheless, the model did not account for fuel sloshing. Furthermore, the controller design did not fully exploit the time-varying behavior of the inherent dynamics.

From an Attitude and Orbit Control System (AOCS)/GNC perspective, OOS missions are particularly demanding due to the time-varying and coupled flexible dynamics of the system. Due to these challenges, the success of on-orbit servicing missions is constrained by the ability to accurately model the system and use advanced analysis tools to predict worst-case scenarios during a preliminary design phase. This is critical as it helps ensure that the control system and other mission critical components are able to handle the unique and complex dynamics of the system and that any potential issues are identified and addressed before the mission is undertaken. When modeling spacecraft dynamics, it is crucial to consider the effects of flexible components, such as solar panels, and vibrational components, like fuel slosh. These can have a significant impact on the spacecraft's behavior. In the context of an OOS mission, the movement of fuel within the tank, known as fuel sloshing, can have an even more pronounced effect on the spacecraft's attitude and pointing. A lumped mechanical multi-mode model that subdivides the fuel in several particles is proposed in [8] and considered in this paper. Since these missions are to take place in microgravity conditions, it is assumed that the fuel is distributed around the inner walls of the fuel tanks, leaving an empty sphere at the center.

The Two-Input Two-Output Ports (TITOP) approach [9] was used to build a Linear Parameter-Varying (LPV) model of two complex multibody mechanical systems, while keeping the uncertain nature of the plant and condensing all possible mechanical configurations in a single low order linear fractional representation (LFR). This framework is a multi-body approach which can connect multiple flexible sub-structures through dynamic ports [10, 11]. It considers uncertain parameters and all possible configurations (changes in mechanical properties, changes in geometric configurations like the rotation angle of a solar array, changes in reaction wheel speed, etc.) in a single LFR. After being constructed using the TITOP approach, the models are prepared for robust control synthesis, along with robust stability and performance evaluation. These models have been implemented in the latest version of the Satellite Dynamics Toolbox Library (SDTlib) [12], which enables users to easily build a model of a flexible spacecraft.

In this context, this paper presents a comprehensive approach for planning and designing an on-orbit servicing mission scenario from an end-to-end perspective, taking into account the structure and control aspects. The authors aim to consider the challenges of flexibility, system uncertainty, sloshing dynamics and time-varying dynamics in the design of a robust controller for an orbital servicing operation. As on-orbit operations of large and flexible structures become more common in future space missions, this approach is increasingly relevant for ensuring the success of these kinds of scenarios.

2 MULTIBODY MODELING APPROACH

2.1 The TITOP approach

The link $\mathcal{L}_i$ connected to the parent substructure $\mathcal{L}_{i-1}$ at the point P_i and to the child substructure $\mathcal{L}_{i+1}$ at the point C_i is depicted in Fig. 1a. The double-port or TITOP model $\left[\mathbf{T}^{\mathcal{L}_i}_{P_i,C_i}\right]_{\mathcal{R}_i}$ is a linear dynamic model between 12 inputs:

- the six components in $\mathcal{R}_i = (P_i^0; x_i, y_i, z_i)$ of the wrench $\left[\mathbf{W}_{\mathcal{L}_{i+1}/\mathcal{L}_i,C_i}\right]_{\mathcal{R}_i} = \begin{bmatrix} \mathbf{F}_{\mathcal{L}_{i+1}/\mathcal{L}_i,C_i} \\ \mathbf{T}_{\mathcal{L}_{i+1}/\mathcal{L}_i,C_i} \end{bmatrix}_{\mathcal{R}_i}$ applied by the substructure $\mathcal{L}_{i+1}$ to the link $\mathcal{L}_i$ at the point C_i: $\mathbf{F}_{\mathcal{L}_{i+1}/\mathcal{L}_i,C_i}$ stands for the three-component force vector applied by $\mathcal{L}_{i+1}$ to $\mathcal{L}_i$ and $\mathbf{T}_{\mathcal{L}_{i+1}/\mathcal{L}_i,C_i}$ stands for the three-component torque vector applied at the point C_i.

- the six components in $\mathcal{R}_i$ of the acceleration twist $[\ddot{\mathbf{x}}_{P_i}]_{\mathcal{R}_i} = \left[\begin{array}{c} \mathbf{a}_{P_i} \\ \dot{\boldsymbol{\omega}}_{P_i} \end{array}\right]_{\mathcal{R}_i}$ of point P_i: $\mathbf{a}_{P_i}$ stands for the three-component linear acceleration vector at the point P_i and $\dot{\boldsymbol{\omega}}_{P_i}$ stands for the three-component angular acceleration vector at the point P_i.

and 12 outputs:

- the six components in $\mathcal{R}_i$ of the acceleration twist $[\ddot{\mathbf{x}}_{C_i}]_{\mathcal{R}_i} = \left[\begin{array}{c} \mathbf{a}_{C_i} \\ \dot{\boldsymbol{\omega}}_{C_i} \end{array}\right]_{\mathcal{R}_i}$.
- the six components in $\mathcal{R}_i$ of the wrench $\left[\mathbf{W}_{\mathcal{L}_i/\mathcal{L}_{i-1},P_i}\right]_{\mathcal{R}_i} = \left[\begin{array}{c} \mathbf{F}_{\mathcal{L}_i/\mathcal{L}_{i-1},P_i} \\ \mathbf{T}_{\mathcal{L}_i/\mathcal{L}_{i-1},P_i} \end{array}\right]_{\mathcal{R}_i}$ that is applied by the link $\mathcal{L}_i$ to the substructure $\mathcal{L}_{i-1}$ at the point P_i.

and can be represented by the block-diagram depicted in Fig. 1b. The TITOP model displayed in Fig. 1 is composed of the direct dynamic model (transfer from acceleration twist to wrench) at the point P_i and the inverse dynamic model (transfer from wrench to acceleration twist) at the point C_i.

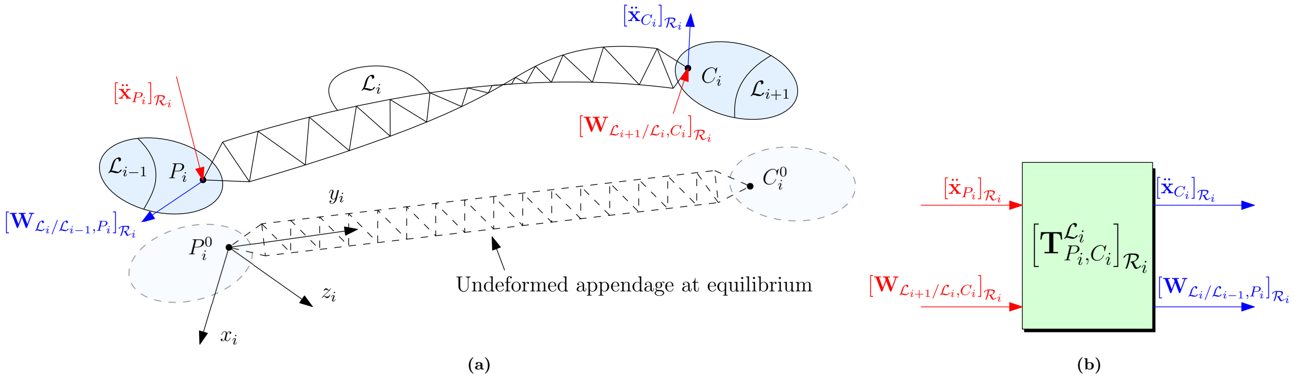

(a)

(b)

Figure 1: (a) i-th flexible appendage of a complex sub-structured body. (b) TITOP model $\left[\mathbf{T}^{\mathcal{L}_i}_{P_i,C_i}\right]_{\mathcal{R}_i}$ block-diagram.

2.2 System modeling

For the on-orbit servicing mission scenario being studied in this paper, two different spacecraft are considered, the chaser and the target, which can be observed in Fig. 2. The chaser is composed of a rigid hub, two symmetric flexible solar arrays, one robotic arm and six fuel particles. The target vehicle consists of a rigid hub, two flexible solar arrays and six fuel particles. The scenario chosen to demonstrate the capabilities of the proposed approach is the target manipulation phase. The latter consists of the chaser manipulating the target with a robotic arm with the objective of performing maintenance or to use it as a mission extension pod. This is just one example scenario and the same approach can be applied to explore a multitude of other mission concepts. For a better understanding of the mission scenario being studied, Fig. 3 depicts three different instants of the coupled system during the whole final rendezvous phase.

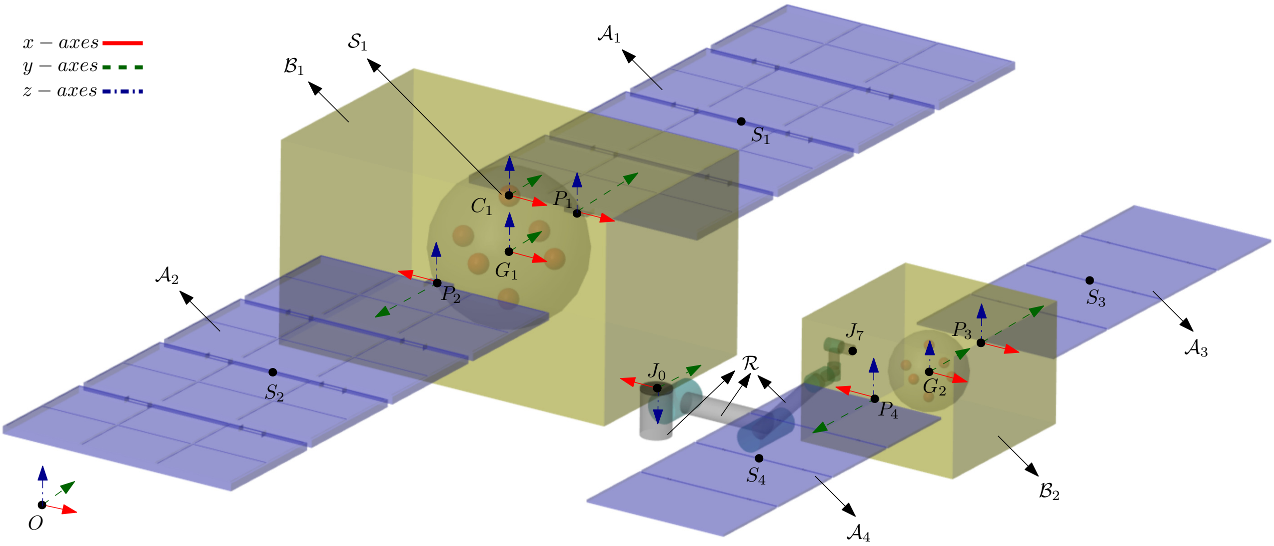

Figure 2: Chaser and target spacecraft composed of two rigid hubs, four solar arrays, one robotic arm and twelve fuel particles (Note: for the sake of simplicity, the x-axes are displayed in solid red lines, the y-axes in dashed green lines and the z-axes in dash-dotted blue lines).

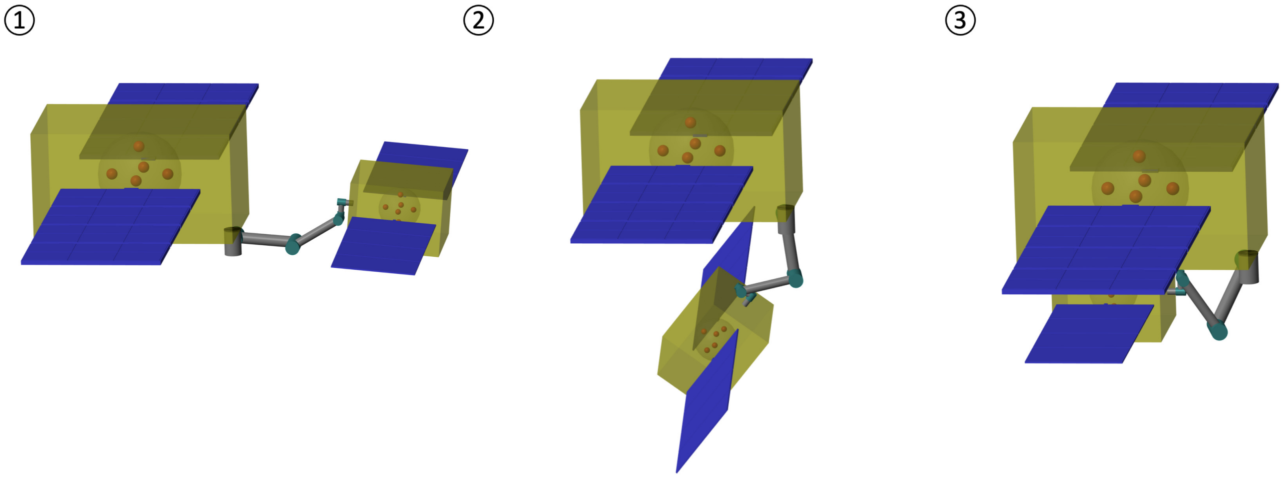

Figure 3: Three different instants of the coupled system during the OOS mission scenario being studied: ①, ② and ③ the robotic arm is docked to the target spacecraft and it is bringing it closer to the chaser's rigid hub.

2.2.1 N-port model of a rigid body

Let us consider a general rigid body $\mathcal{B}$ with center of mass G. Considering that the rigid body is submitted to external forces/moments $\mathbf{F}_{\text{ext}/\mathcal{B},G}$, $\mathbf{T}_{\text{ext}/\mathcal{B},G}$ (i.e. solar radiation pressure, gravity gradient, atmospheric drag, magnetic fields, etc.) and to forces/moments $\mathbf{F}_{\mathcal{B}/\mathcal{A},P}$, $\mathbf{T}_{\mathcal{B}/\mathcal{A},P}$ due to interactions with an appendage $\mathcal{A}$ connected at the point P, the linearized Newton-Euler equations read:

$$\underbrace{\begin{bmatrix}\mathbf{F}_{\text{ext}/\mathcal{B},G}-\mathbf{F}_{\mathcal{B}/\mathcal{A},G}\\ \mathbf{T}_{\text{ext}/\mathcal{B},G}-\mathbf{T}_{\mathcal{B}/\mathcal{A},G}\end{bmatrix}}_{\mathbf{W}_{\text{ext}/\mathcal{B},G}-\mathbf{W}_{\mathcal{B}/\mathcal{A},G}} = \mathbf{D}_G^{\mathcal{B}} \underbrace{\begin{bmatrix}\mathbf{a}_G\\ \dot{\boldsymbol{\omega}}_G\end{bmatrix}}_{\ddot{\mathbf{x}}_G} \quad \text{with} \quad \mathbf{D}_G^{\mathcal{B}} = \begin{bmatrix} m_{\mathcal{B}}\mathbf{I}_3 & \mathbf{0}_{3\times3}\\ \mathbf{0}_{3\times3} & \mathbf{J}_G^{\mathcal{B}}\end{bmatrix} \tag{1}$$

where $\mathbf{D}_G^{\mathcal{B}}$ is the static direct dynamic model of $\mathcal{B}$ at the body's center of mass G and $\mathbf{a}_G$ is the linear acceleration vector of $\mathcal{B}$ at G. Furthermore, $m_{\mathcal{B}}$ is the mass of $\mathcal{B}$ and $\mathbf{J}_G^{\mathcal{B}}$ represents the inertia tensor of $\mathcal{B}$ written in the body frame of the rigid body $\mathcal{R}_{\mathcal{B}} = (G; x_G, y_G, z_G)$. The mathematical relation between the wrenches $\mathbf{W}_{\mathcal{B}/\mathcal{A},G}$, $\mathbf{W}_{\mathcal{B}/\mathcal{A},P}$ and the acceleration twists $\ddot{\mathbf{x}}_G$, $\ddot{\mathbf{x}}_P$ is given by:

$$\underbrace{\begin{bmatrix} \mathbf{F}_{\mathcal{B}/\mathcal{A},G} \\ \mathbf{T}_{\mathcal{B}/\mathcal{A},G} \end{bmatrix}}_{\mathbf{W}_{\mathcal{B}/\mathcal{A},G}} = \boldsymbol{\tau}_{PG}^{\mathrm{T}} \underbrace{\begin{bmatrix} \mathbf{F}_{\mathcal{B}/\mathcal{A},P} \\ \mathbf{T}_{\mathcal{B}/\mathcal{A},P} \end{bmatrix}}_{\mathbf{W}_{\mathcal{B}/\mathcal{A},P}} \quad \text{and} \quad \underbrace{\begin{bmatrix} \mathbf{a}_P \\ \dot{\boldsymbol{\omega}}_P \end{bmatrix}}_{\ddot{\mathbf{x}}_P} = \boldsymbol{\tau}_{PG} \underbrace{\begin{bmatrix} \mathbf{a}_G \\ \dot{\boldsymbol{\omega}}_G \end{bmatrix}}_{\ddot{\mathbf{x}}_G} \tag{2}$$

where $\boldsymbol{\tau}_{PG}$ describes the rigid kinematic model between the degrees of freedom (DOF) of point P and the DOF of point G. It is given by:

$$\boldsymbol{\tau}_{PG} = \begin{bmatrix} \mathbf{I}_3 & (^*\mathbf{r}_{PG}) \\ \mathbf{0}_{3\times3} & \mathbf{I}_3 \end{bmatrix} \quad \text{with} \quad (^*\mathbf{r}_{PG}) = \begin{bmatrix} 0 & -z & y \\ z & 0 & -x \\ -y & x & 0 \end{bmatrix} \quad \text{and} \quad \mathbf{r}_{PG} = \begin{bmatrix} x \\ y \\ z \end{bmatrix} \tag{3}$$

From Eqs. (1) and (2), the TITOP model of a rigid body $\mathcal{B}$ connected to n appendages can directly be obtained:

$$\begin{bmatrix} \ddot{\mathbf{x}}_{P_1} \\ \ddot{\mathbf{x}}_{P_2} \\ \vdots \\ \ddot{\mathbf{x}}_{P_n} \\ \ddot{\mathbf{x}}_G \end{bmatrix} = \underbrace{\begin{bmatrix} \boldsymbol{\tau}_{P_1G} \\ \boldsymbol{\tau}_{P_2G} \\ \vdots \\ \boldsymbol{\tau}_{P_nG} \\ \mathbf{I}_6 \end{bmatrix} \left[\mathbf{D}_G^{\mathcal{B}}\right]^{-1} \begin{bmatrix} \boldsymbol{\tau}_{P_1G}^{\mathrm{T}} & \boldsymbol{\tau}_{P_2G}^{\mathrm{T}} & \cdots & \boldsymbol{\tau}_{P_nG}^{\mathrm{T}} & \mathbf{I}_6 \end{bmatrix}}_{\left[\tilde{\mathbf{D}}_{P_1\ldots P_nG}^{\mathcal{B}}\right]^{-1}} \begin{bmatrix} \mathbf{W}_{\mathcal{A}_1/\mathcal{B},P_1} \\ \mathbf{W}_{\mathcal{A}_2/\mathcal{B},P_2} \\ \vdots \\ \mathbf{W}_{\mathcal{A}_n/\mathcal{B},P_n} \\ \mathbf{W}_{\mathrm{ext}/\mathcal{B},G} \end{bmatrix} \tag{4}$$

where $\left[\tilde{\mathbf{D}}_{P_1\ldots P_nG}^{\mathcal{B}}\right]^{-1}$ is the multi-port inverse linearized dynamic model of the rigid body $\mathcal{B}$ computed at the points $P_1, \ldots, P_n, G$ in the body frame $\mathcal{R}_{\mathcal{B}}$. This model can also be computed when one of the ports is inverted (transfer from acceleration twist to wrench). In that case:

$$\tilde{\mathbf{D}}_{P_1\ldots P_nG}^{\mathcal{B}} = \begin{bmatrix} \boldsymbol{\tau}_{GP_1}^{\mathrm{T}} \begin{bmatrix} -\mathbf{D}_G^{\mathcal{B}}\boldsymbol{\tau}_{GP_1} & \boldsymbol{\tau}_{P_2G}^{\mathrm{T}} & \cdots & \boldsymbol{\tau}_{P_nG}^{\mathrm{T}} & \mathbf{I}_6 \end{bmatrix} \\ \begin{bmatrix} \boldsymbol{\tau}_{P_2G} \\ \vdots \\ \boldsymbol{\tau}_{P_nG} \\ \mathbf{I}_6 \end{bmatrix} \begin{bmatrix} \boldsymbol{\tau}_{GP_1} & \mathbf{0}_{6\times6} & \cdots & \mathbf{0}_{6\times6} & \mathbf{0}_{6\times6} \end{bmatrix} \end{bmatrix} \tag{5}$$

where $\tilde{\mathbf{D}}_{P_1\ldots P_nG}^{\mathcal{B}}$ represents the multi-port direct/inverse linearized dynamic model of the rigid body $\mathcal{B}$: inverse linearized dynamic model computed at the points $P_2, \ldots, P_n, G$ and linearized direct dynamic model (with a minus sign) computed at the point P_1 in the body frame $\mathcal{R}_{\mathcal{B}}$. One of the objectives of this paper is to demonstrate how to design a controller in the presence of significant model uncertainty. As an example, let us now consider the mass of the rigid body $m_{\mathcal{B}}$ uncertain, with $m_{\mathcal{B}} = m_{\mathcal{B}_0}(1 + r_{m_{\mathcal{B}}}\delta_{m_{\mathcal{B}}})$. In this case, $m_{\mathcal{B}_0}$ is the body's nominal mass, $r_{m_{\mathcal{B}}}$ is used to set the maximum percent of variation for the body's mass and $\delta_{m_{\mathcal{B}}} \in [-1, 1]$ is a normalized real uncertainty, which appears three times in the minimal LFR of a rigid body [12]. Therefore, the uncertainty block regarding the mass of $\mathcal{B}$ is equal to $\boldsymbol{\Delta}_{m_{\mathcal{B}}} = \delta_{m_{\mathcal{B}}}\mathbf{I}_3$.

2.2.2 Model of a general flexible appendage

A general flexible appendage $\mathcal{A}$ connected to a parent rigid body $\mathcal{B}$ at the point P is considered. The effective mass model of the appendage $-\mathbf{M}_P^{\mathcal{A}}(s)$ establishes a connection between the six DOF acceleration vector of point P and the six DOF forces/moments vector applied by the appendage $\mathcal{A}$ to the parent body at the point P:

$$\left[\begin{array}{c}\dot{\boldsymbol{\eta}}\\ \ddot{\boldsymbol{\eta}}\\ \hline \mathbf{W}_{\mathcal{A}/\mathcal{B},P}\end{array}\right] = \underbrace{\left[\begin{array}{cc|c} \mathbf{0}_{N\times N} & \mathbf{I}_N & \mathbf{0}_{N\times 6}\\ -\operatorname{diag}\left(\omega_{i_\mathcal{A}}^2\right) & -\operatorname{diag}\left(2\zeta_{i_\mathcal{A}}\omega_{i_\mathcal{A}}\right) & -\mathbf{L}_P^{\mathcal{A}} \\ \hline -\mathbf{L}_P^{\mathcal{A}^{\mathrm{T}}}\operatorname{diag}\left(\omega_{i_\mathcal{A}}^2\right) & -\mathbf{L}_P^{\mathcal{A}^{\mathrm{T}}}\operatorname{diag}\left(2\zeta_{i_\mathcal{A}}\omega_{i_\mathcal{A}}\right) & \mathbf{D}_{P_0}^{\mathcal{A}}\end{array}\right]}_{-\mathbf{M}_P^{\mathcal{A}}(s)} \left[\begin{array}{c}\boldsymbol{\eta}\\ \dot{\boldsymbol{\eta}}\\ \hline \ddot{\mathbf{x}}_P\end{array}\right] \tag{6}$$

where $\omega_{i_\mathcal{A}}$, $\xi_{i_\mathcal{A}}$ and $\boldsymbol{l}_{i,P}^{\mathcal{A}}$ are the natural frequency, the damping ratio and the 6 DOF participation factor vector of the i-th flexible mode of the appendage $\mathcal{A}$, $\mathbf{L}_P^{\mathcal{A}} = \left[\boldsymbol{l}_{1,P}^{\mathcal{A}}, \ldots, \boldsymbol{l}_{i,P}^{\mathcal{A}}, \ldots, \boldsymbol{l}_{N,P}^{\mathcal{A}}\right]$ is the matrix of modal participation factors of the N flexible modes of the appendage at the point P, $\mathbf{D}_{P_0}^{\mathcal{A}} = \mathbf{D}_P^{\mathcal{A}} - \Sigma_{i=1}^{N}\mathbf{M}_{i,P}^{\mathcal{A}} = \mathbf{D}_P^{\mathcal{A}} - \mathbf{L}_P^{\mathcal{A}}\mathbf{L}_P^{\mathcal{A}^{\mathrm{T}}}$ is the 6-by-6 residual mass/inertia of the appendage rigidly cantilevered to the parent body $\mathcal{B}$ at the point P, $\mathbf{M}_{i,P}^{\mathcal{A}} = \boldsymbol{l}_{i,P}^{\mathcal{A}}\mathrm{l}_{i,P}^{\mathcal{A}^{\mathrm{T}}}$ is the 6-by-6 effective mass/inertia matrix of the i-th flexible mode of the appendage and s is the Laplace variable. The static model of the appendage $\mathbf{D}_P^{\mathcal{A}}$ computed at the attachment point P is given by:

$$\mathbf{D}_P^{\mathcal{A}} = \boldsymbol{\tau}_{AP}^{\mathrm{T}}\begin{bmatrix} m_{\mathcal{A}}\mathbf{I}_3 & \mathbf{0}_{3\times 3}\\ \mathbf{0}_{3\times 3} & \mathbf{J}_A^{\mathcal{A}}\end{bmatrix}\boldsymbol{\tau}_{AP} \tag{7}$$

where $m_{\mathcal{A}}$ is the mass of $\mathcal{A}$ and $\mathbf{J}_A^{\mathcal{A}}$ represents the inertia tensor of $\mathcal{A}$ written in the appendage's body frame $\mathcal{R}_{\mathcal{A}} = (P; x_P, y_P, z_P)$ and expressed at its center of mass A.

2.2.3 Connection model between two different bodies

The inverse dynamic model of a rigid body described in Eq. (4) is expressed in the body frame $\mathcal{R}_{\mathcal{B}} = (G; x_G, y_G, z_G)$. On the other hand, the model of a general flexible appendage represented in Eq. (6) is expressed in the appendage frame $\mathcal{R}_{\mathcal{A}} = (P; x_P, y_P, z_P)$. A Direct Cosine Matrix (DCM) $\mathcal{T}_{\mathcal{R}_{\mathcal{B}}/\mathcal{R}_{\mathcal{A}}}$ is thus needed to connect the two models. $\mathcal{T}_{\mathcal{R}_{\mathcal{B}}/\mathcal{R}_{\mathcal{A}}}$ is nothing else than the matrix of components of the unitary vectors x_P, y_P, z_P expressed in $\mathcal{R}_{\mathcal{B}}$. The DCM $\mathcal{T}_{\mathcal{R}_{\mathcal{B}}/\mathcal{R}_{\mathcal{A}}}$ has a constant value if the appendage is fixed in a certain angular orientation with respect to the rigid body $\mathcal{B}$. However, if the appendage rotates around a certain direction vector $\mathbf{v}$, the required transformation matrix has to be parameterized according to the time-varying rotation angle α. In this case, the rotation matrix will be represented as $\mathcal{T}_\alpha$. If the unit vectors z_P and z_G are aligned and the appendage $\mathcal{A}$ rotates around $\mathbf{v} \equiv z_P \equiv z_G$, $\mathcal{T}_\alpha$ can be written as follows:

$$\mathcal{T}_\alpha = \begin{bmatrix} \cos(\alpha) & -\sin(\alpha) & 0\\ \sin(\alpha) & \cos(\alpha) & 0\\ 0 & 0 & 1\end{bmatrix} \tag{8}$$

An LFT parameterization of the rotation matrix described in Eq. (8) is implemented as demonstrated by Guy et al. [13], with $\tau_\alpha = \tan(\alpha/4)$ and $\tau_\alpha \in [-1, 1]$. The complete block-diagram model of the connection between a rigid body $\mathcal{B}$ and an appendage $\mathcal{A}$ is displayed in Fig. 4a. The transformation model $\mathcal{R}_\alpha$ can be observed in Fig. 4b.

2.2.4 Sloshing model

The behaviour of fluid within a spherical tank is investigated by dividing the fuel in several particles. Each particle is connected to three sets of springs and dampers, each set oriented along one of the three mutually perpendicular axes in three-dimensional space ($\mathbf{x}$, $\mathbf{y}$ and $\mathbf{z}$ directions), as follows:

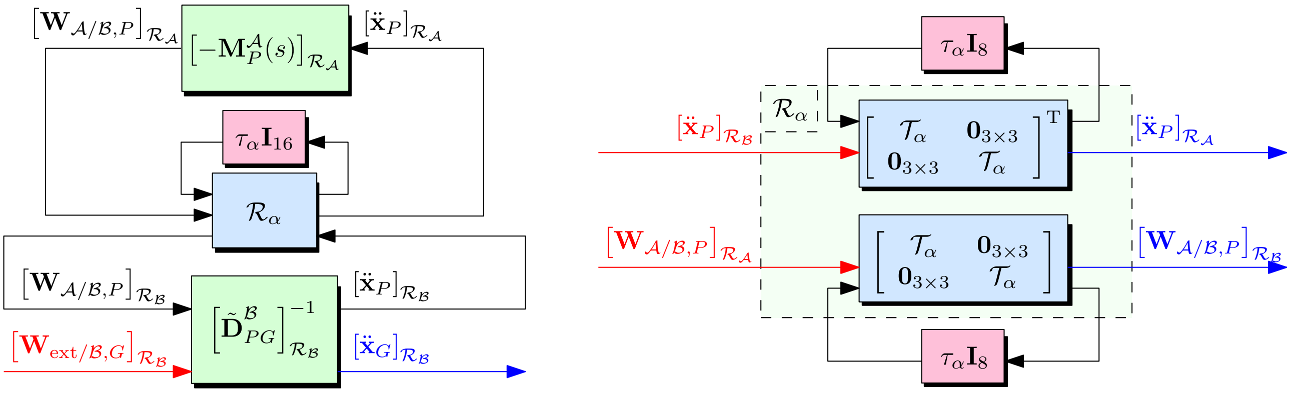

(a) (b)

Figure 4: (a) Block-diagram model of the connection between a rigid body $\mathcal{B}$ and an appendage $\mathcal{A}$. (b) Assembly of the transformation model $\mathcal{R}_\alpha$.

$$\begin{cases} m_\mathcal{S}\mathbf{I}_3\left(\mathbf{a}_C + \delta\ddot{\mathbf{r}}_\mathcal{S}\right) = -k_\mathcal{S}\mathbf{I}_3\delta\mathbf{r}_\mathcal{S} - c_\mathcal{S}\mathbf{I}_3\delta\dot{\mathbf{r}}_\mathcal{S} \\ \mathbf{F}_{\mathcal{S}/\mathcal{B},C} = k_\mathcal{S}\mathbf{I}_3\delta\mathbf{r}_\mathcal{S} + c_\mathcal{S}\mathbf{I}_3\delta\dot{\mathbf{r}}_\mathcal{S} \end{cases} \tag{9}$$

In Eq. (9), $m_\mathcal{S}$, $k_\mathcal{S}$ and $c_\mathcal{S}$ are the mass of the fuel particle, the springs stiffness and the springs damping coefficient, respectively. Furthermore, $\delta\mathbf{r}_\mathcal{S} = \begin{bmatrix} \delta x_\mathcal{S} & \delta y_\mathcal{S} & \delta z_\mathcal{S} \end{bmatrix}^\mathrm{T}$ represents the displacement or change in position of the fuel particle from its equilibrium position in the 3 different directions. This model shows that a horizontal or lateral motion of the spacecraft body $\mathcal{B}$ causes the liquid to slosh (i.e., causes the sprung mass of the model to oscillate relative to the body). Fig. 5a shows the block-diagram of the lateral sloshing model $\mathbf{N}_C^\mathcal{S}(s)$ described in Eq. (9). This model is written in the inherit body frame, meaning that $\mathcal{R}_\mathcal{S} \equiv \mathcal{R}_\mathcal{B}$. Furthermore, Fig. 5b illustrates a scenario where a fuel particle is situated in a massless spherical tank, which in turn is enclosed within a rigid spacecraft $\mathcal{B}$. In this situation, it is considered that the particle only moves along the x-axis, and it is possible to see what happens when the sloshing mass moves around its equilibrium position located at the point C.

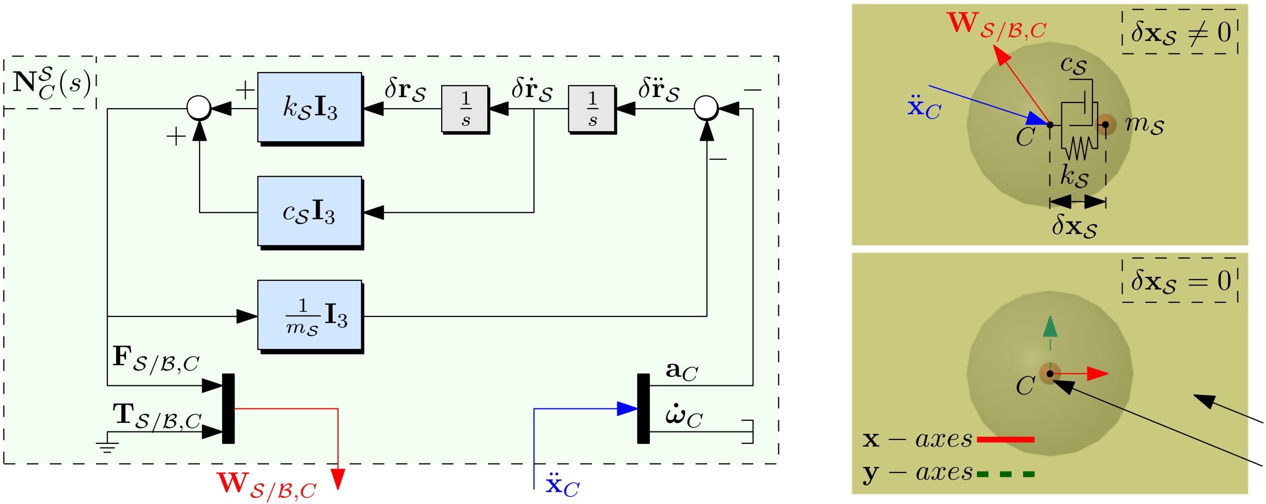

(a) (b)

Figure 5: (a) Block-diagram of the lateral sloshing model. (b) Illustration of a scenario where a fuel particle is situated in a massless spherical tank, which in turn is enclosed within a rigid spacecraft $\mathcal{B}$.

2.2.5 Complete model of the system

A global LFR representation is obtained, minimal in terms of mechanical parameter occurrences. This model fully captures the dynamics and interactions between all the subsystems of the OOS scenario being studied: robotic arm, flexible appendages and sloshing dynamics. Furthermore, it also takes into account the various uncertainty effects in a very compact representation. Fig. 6 illustrates the internal structure of the overall LFR model as well as the interconnections between the several subsystems. In this representation, all the block uncertainties are isolated at the component level.

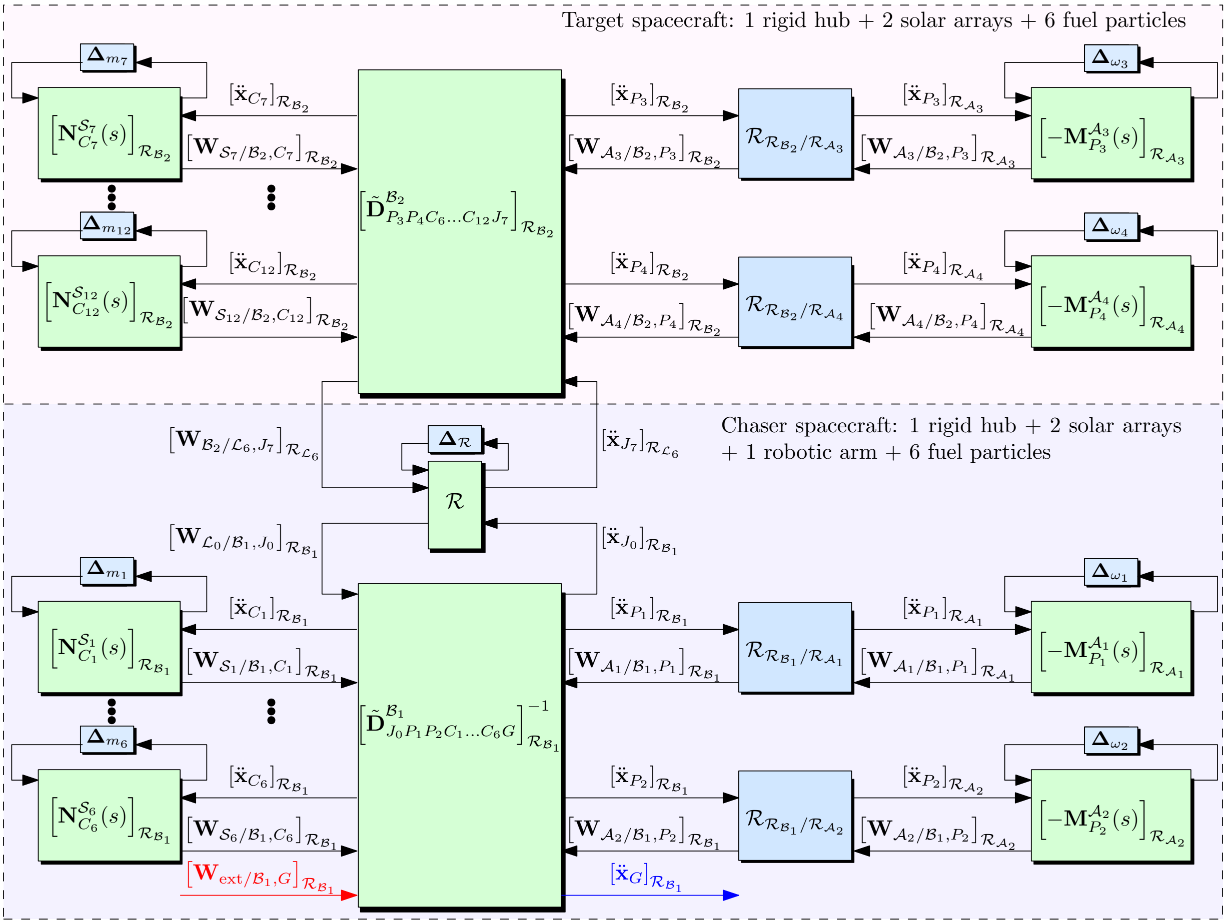

Figure 6: Block-diagram of the uncertain plant written in LFR form.

The notation used in Fig. 6 is defined according to Fig. 2 and all the different dynamic models computed before. The presented approach considers the fuel in each spacecraft to be divided in 6 particles placed symmetrically around the surface of the tanks, as depicted in Fig. 2. Relative uncertainty is taken into account on the mass of the particles $m_{\mathcal{S}_\bullet}$, where $\mathbf{\Delta}_{m_\bullet} = \delta_{m_{\mathcal{S}_\bullet}} \mathbf{I}_3$, and on the natural frequencies of all the solar arrays' first flexible modes $\omega_{1_{\mathcal{A}_\bullet}}$, with $\mathbf{\Delta}_{\omega_\bullet} = \delta_{\omega_{1_{\mathcal{A}_\bullet}}} \mathbf{I}_2$. Furthermore, $\mathbf{\Delta}_{mod} = \text{diag}\left(\mathbf{\Delta}_{\omega_1}, \mathbf{\Delta}_{\omega_2}, \mathbf{\Delta}_{\omega_3}, \mathbf{\Delta}_{\omega_4}\right)$ and $\mathbf{\Delta}_{slosh} = \text{diag}\left(\mathbf{\Delta}_{m_1}, \mathbf{\Delta}_{m_2}, \ldots, \mathbf{\Delta}_{m_{11}}, \mathbf{\Delta}_{m_{12}}\right)$. The chaser spacecraft also uses a robotic arm $\mathcal{R}$ for manipulating the target on-orbit. This arm manipulator, which is composed of 7 links and 6 joints, is exactly the one used in [7], where $\alpha_\bullet$ represents the arm's angular configuration. The uncertainty block describing the changing geometrical configuration of the robotic arm is given by $\mathbf{\Delta}_{\mathcal{R}} = \text{diag}\left(\mathbf{\Delta}_{\alpha_1}, \mathbf{\Delta}_{\alpha_2}, \mathbf{\Delta}_{\alpha_3}, \mathbf{\Delta}_{\alpha_4}, \mathbf{\Delta}_{\alpha_5}, \mathbf{\Delta}_{\alpha_6}\right)$, with $\mathbf{\Delta}_{\alpha_\bullet} = \tau_{\alpha_\bullet} \mathbf{I}_{16}$ and $\tau_{\alpha_\bullet} \in [-1, 1]$. Fifth-order polynomials are generated for the trajectories of the robotic arm joint angles. These trajectories are defined in terms of $\tau_{\alpha_\bullet}$, with $\tau_{\alpha_\bullet} = a_\bullet + b_\bullet t + c_\bullet t^2 + d_\bullet t^3 + e_\bullet t^4 + f_\bullet t^5 = a_\bullet + t\left(b_\bullet + t\left(c_\bullet + t\left(d_\bullet + t\left(e_\bullet + t f_\bullet\right)\right)\right)\right)$. The coefficients of the polynomials that were obtained for

$\tau_{\alpha_\bullet}$ result in 400 occurrences of the time parameter t. All the numerical values and range of variations of the numerous system parameters which are employed in this section are described in Table 1. The reader should refer to [7] for more information about the arm manipulator. Thanks to the latest SDTlib [12] release, it is possible to assemble the complete system displayed in Fig. 6 in a *Simulink* environment. Utilizing the SDTlib offers the possibility of declaring the parameters in each subsystem as uncertain. A minimal LFT can then be obtained, enabling direct use in linear robust controller synthesis and assessment of robust stability and performance.

2.3 Analysis of the system dynamics

By setting the varying parameters $\alpha_\bullet$ accordingly, the singular values of the system shown in Fig. 6 are analyzed at the three different instants depicted in Fig. 3. Initially, the transfer function between $\mathbf{T}_{\text{ext}/\mathcal{B}_1,G_1}\{2\}$ and $\dot{\boldsymbol{\omega}}_{G_1}\{2\}$ is examined for the nominal system ($\mathbf{T}_{\text{ext}/\mathcal{B}_1,G_1}\{2\} \rightarrow \dot{\boldsymbol{\omega}}_{G_1}\{2\}$ channel). According to the modal participation factor matrices $\mathbf{L}_{P_\bullet}^{A_\bullet}$ definition [13], the plot depicted in Fig. 7 is consistent with the properties of both spacecraft's flexible elements. The corresponding antiresonances occur at the frequencies of the solar arrays' cantilevered flexible modes (see Table 1). Moreover, it is assumed that the fuel particles in the same spacecraft have the same mass under nominal conditions. Furthermore, the spring-damper properties $k_{\mathcal{S}}$ and $c_{\mathcal{S}}$ are also assumed to be the same in all directions. The antiresonance frequencies regarding the sloshing dynamics are equal to $\omega_{\mathcal{S}} = \sqrt{\frac{k_{\mathcal{S}}}{m_{\mathcal{S}}}}$, with a corresponding damping ratio of $\xi_{\mathcal{S}} = \frac{c_{\mathcal{S}}}{2m_{\mathcal{S}}\omega_{\mathcal{S}}}$. Therefore, the chaser's sloshing natural frequencies are equal to $\omega_{\mathcal{S}_{1-6}} = 0.1368$ Hz and the target's sloshing natural frequencies are equivalent to $\omega_{\mathcal{S}_{7-12}} = 0.1529$ Hz in nominal conditions, as can be observed in Fig. 7. The same figure also depicts the effect that the subsets of real parametric uncertainty $\boldsymbol{\Delta}_{mod}$ and $\boldsymbol{\Delta}_{slosh}$ have on the singular values of the same transfer function.

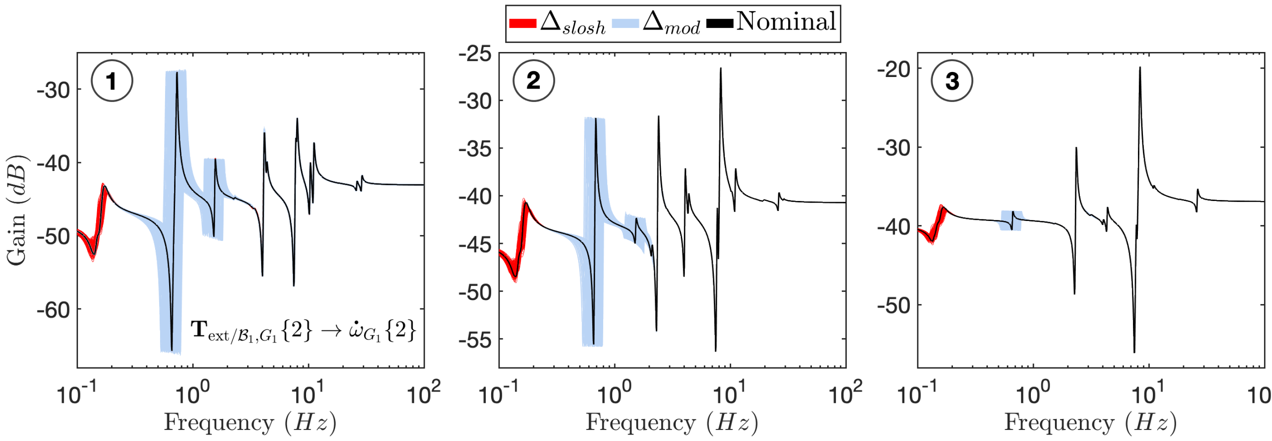

Figure 7: Gains of the uncertain and nominal systems for the three instants displayed in figure 3 ($\mathbf{T}_{\text{ext}/\mathcal{B}_1,G_1}\{2\} \rightarrow \dot{\boldsymbol{\omega}}_{G_1}\{2\}$ transfer function).

3 CONTROL ARCHITECTURE AND SYNTHESIS METHODOLOGY

Some of the challenges of an OOS mission scenario include the control structure interactions between the flexible appendages/sloshing and the AOCS, the time-varying inertial properties, the flexible dynamics, the system uncertainties and also the dynamic couplings. Only attitude control design is addressed, since this paper's objective is to focus on the target spacecraft manipulation phase.

3.1 Gain-scheduled $\mathcal{H}_\infty$ control

In order to design a control law that accommodates the desired performance requirements, the synthesis problem is recast into the nonsmooth $\mathcal{H}_\infty$ framework [14] by first assembling the weighted interconnection shown in Fig. 8a. This model is used to design an LPV gain-scheduled controller [11, 15], where the scheduling variable is the time t. A low order global uncertainty block system is built in a very straightforward way by just concatenating the individual uncertainty blocks, with $\mathbf{\Delta_P} = \mathrm{diag}\left(\mathbf{\Delta}_{mod}, \mathbf{\Delta}_{slosh}\right)$. The plant model $\mathbf{P}$ is logically the one represented in Fig. 6. However, only the $\mathbf{T}_{\mathrm{ext}/\mathcal{B}_1,G_1} \rightarrow \dot{\boldsymbol{\omega}}_{G_1}$ channels are considered, since the objective is to design an attitude controller. This interconnection is composed of the following blocks:

Sensor and actuator models: First, the star tracker dynamics $\mathcal{SST}(s)$ correspond to a first order low pass filter with a cutoff frequency of 8 Hz. Secondly, the gyroscope dynamics $\mathcal{GYRO}(s)$ are represented by a first order low pass filter with a 200 Hz cutoff frequency. Finally, the reaction wheel system dynamics $\mathcal{RW}(s)$ are approximated by a second order transfer, with a damping ratio equal to 0.7 and a natural frequency of 200 Hz.

Disturbance weights: The measurement noise weights $\mathbf{W}_{n,gyro}$ and $\mathbf{W}_{n,sst}$ are used to define the upper bounds on the expected amplitude spectral density (ASD) of the closed-loop noise measurements. In this case, $\mathbf{W}_{n,gyro} = 9.1987 \times 10^{-4}\mathbf{I}_3\ \mathrm{rad}^2\ \mathrm{s}^{-1}$ and $\mathbf{W}_{n,sst} = 1.5343 \times 10^{-5}\mathbf{I}_3\ \mathrm{rad}^2\ \mathrm{s}$. Similarly, the purpose of the weight $\mathbf{W}_{n,ext}(s) = \mathrm{diag}\left(\frac{0.002577}{2.236s+0.2236}, \frac{0.009685}{2.236s+0.2236}, \frac{0.01239}{2.236s+0.2236}\right)\ \mathrm{N\,m}$ is to model the upper bound on the expected closed-loop orbital and robotic arm disturbances at different frequencies.

Performance weights: The purpose of the weight $\mathbf{W}_u = \mathrm{diag}\left(0.8333,\ 0.8333,\ 0.8333\right)\ \mathrm{N}^{-1}\,\mathrm{m}^{-1}$ is to impose a desired closed-loop upper bound of $1.2\ \mathrm{N\,m}$ on the worst-case actuator signals at different frequencies. Similarly, the objective of the absolute pointing error (APE) requirement $\mathbf{W}_p = \mathrm{diag}\left(35.2113,\ 35.2113,\ 35.2113\right)\ \mathrm{rad}^{-1}$ is to impose an upper bound of $0.0284\ \mathrm{rad}$ on the three different axes.

Roll-off filter: A 4th-order roll-off Butterworth filter $\mathbf{F}_{ro}(s)$ with a cutoff frequency of 0.5 Hz is also added to the output control signal $\mathbf{u}$, ensuring the controller is not sensitive to high frequency content. Finally, the structure that was chosen for the adaptable controller $\widehat{\mathbf{K}}(s,t)$ is:

$$\widehat{\mathbf{K}}(s,t) = \mathcal{F}_u\left(\left[\begin{array}{c|c}\mathbf{A_{K_0}} & \mathbf{B_{K_0}} \\ \hline \mathbf{C_{K_0}} & \mathbf{D_{K_0}}\end{array}\right] + t\left[\begin{array}{c|c}\mathbf{A_{K_1}} & \mathbf{B_{K_1}} \\ \hline \mathbf{C_{K_1}} & \mathbf{D_{K_1}}\end{array}\right], \frac{\mathbf{I}_{n_c}}{s}\right) = \mathcal{F}_l\left(\mathbf{K}(s), t\mathbf{I}_{n_k}\right) \tag{10}$$

with $\mathbf{K}(s) \subset \mathbb{RH}_\infty^{(n_k+n_y)\times(n_k+n_u)}$, where $\mathbb{RH}_\infty^{(n_k+n_y)\times(n_k+n_u)}$ represents the set of finite gain transfer matrices with (n_k+n_y) outputs and (n_k+n_u) inputs. Furthermore, n_c is the order of the controller, n_y is the number of inputs, n_u is the number of outputs, n_k is the number of occurrences of the scheduling parameter t, $\mathcal{F}_u(\cdot)$ represents the upper linear fractional transformation and $\mathcal{F}_l(\cdot)$ is the lower linear fractional transformation. The matrices $\mathbf{A_{K_0}}, \mathbf{A_{K_1}}, \mathbf{B_{K_0}}, \mathbf{B_{K_1}}, \mathbf{C_{K_0}}, \mathbf{C_{K_1}}, \mathbf{D_{K_0}}, \mathbf{D_{K_1}}$ are real matrices of appropriate dimensions. The closed-loop model, denoted $\mathbf{G}(s,t)$, can be observed in Fig. 8b. Furthemore, the uncertain closed-loop model is given by $\widehat{\mathbf{G}}(s,t,\mathbf{\Delta_P}) = \mathcal{F}_u\left(\mathbf{G}(s,t), \mathbf{\Delta_P}\right)$. The following mixed $\mathcal{H}_\infty/\mathcal{H}_2$ problem is solved:

$$\begin{array}{llll} \min\limits_{\mathbf{K}(s)} \quad \gamma_1 & \text{s.t.} \ \sup\limits_{\mathbf{\Delta_P},t} \left\|\widehat{\mathbf{G}}_{\tilde{\mathbf{d}}\rightarrow\mathbf{e}_t}(s,t,\mathbf{\Delta_P})\right\|_2 \leq \gamma_1 & & \text{(soft constraint)} \\ \text{subject to} & \dfrac{1}{\gamma_2} \sup\limits_{\mathbf{\Delta_P},t} \left\|\widehat{\mathbf{G}}_{\mathbf{d}_u\rightarrow\tilde{\mathbf{e}}}(s,t,\mathbf{\Delta_P})\right\|_\infty \leq 1 & & \text{(hard constraint)} \end{array} \tag{11}$$

with $\tilde{\mathbf{e}} = \begin{bmatrix} \mathbf{e}_u \\ \mathbf{e}_p \end{bmatrix}$ and $\tilde{\mathbf{d}} = \begin{bmatrix} \mathbf{d}_{n,sst} \\ \mathbf{d}_{n,gyro} \end{bmatrix}$. $\mathbf{D_{K_0}}$ is initialized with a static controller tuned to the total static inertia of the coupled spacecraft at $t = 0\ \mathrm{s}$ and $\mathbf{A_{K_0}}$, $\mathbf{B_{K_0}}$, $\mathbf{C_{K_0}}$ are initialized with zero matrices. The resulting controller $\widehat{\mathbf{K}}(s,t)$ has $n_c = 4$ states, $n_k = 5$ occurrences of the parameter t and a performance level of $\gamma_2 = 0.9946$, meaning that the hard constraint has been completely satisfied. The gains of $\mathbf{F}_{ro}(s)\widehat{\mathbf{K}}(s,t)$ are shown in Fig. 9 for the channels $\mathbf{y}\{5\} \rightarrow \mathbf{u}_{ro}$ and for different values of $t \in [0,600]$. The three plots exhibit a behavior similar to that of a notch filter. The described behavior occurs at the natural frequencies $\omega_{\mathcal{S}}$ for the channels $\mathbf{y}\{5\} \rightarrow \mathbf{u}_{ro}\{1\}$ and $\mathbf{y}\{5\} \rightarrow \mathbf{u}_{ro}\{3\}$. For the channel $\mathbf{y}\{5\} \rightarrow \mathbf{u}_{ro}\{2\}$, this behavior happens around $\omega_{1_{\mathcal{A}_{3,4}}}$.

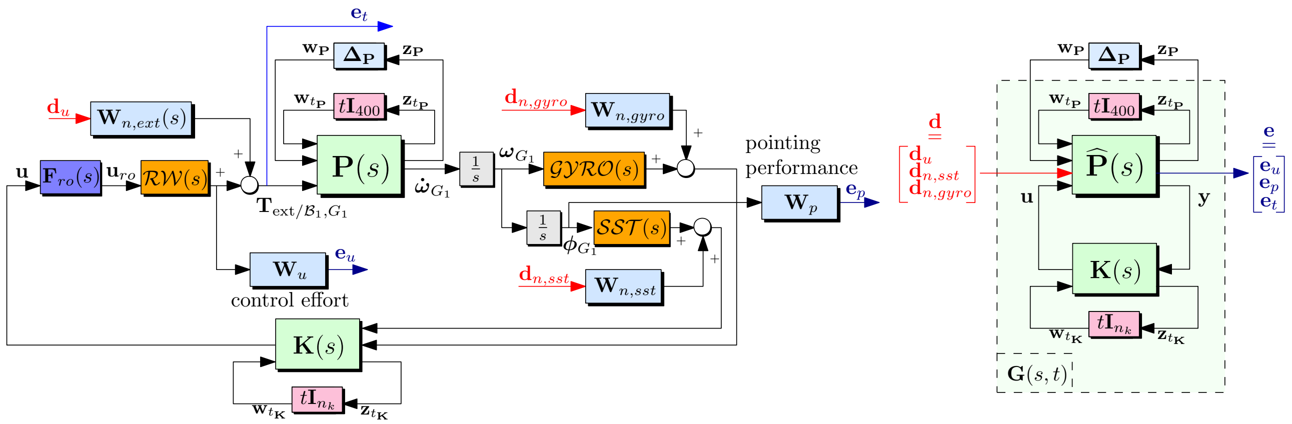

(a)

(b)

Figure 8: (a) System architecture used for controller synthesis and worst-case analysis. (b) Equivalent standard form of the interconnection.

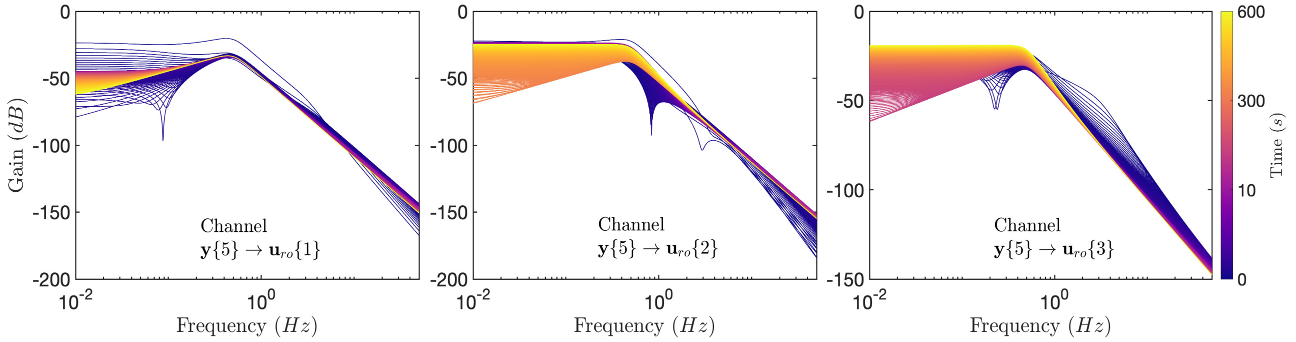

Figure 9: Gains of $\mathbf{F}_{ro}(s)\widehat{\mathbf{K}}(s,t)$ for different values of the scheduling parameter $t \in [0,600]$ ($\mathbf{y}\{5\} \rightarrow \mathbf{u}_{ro}$ transfer functions).

4 PERFORMANCE AND STABILITY ANALYSIS

4.1 Worst-case analysis

The robust stability of the closed-loop interconnection $\widehat{\mathbf{G}}(s,t,\boldsymbol{\Delta}_\mathbf{P})$ is evaluated. This assessment is done by computing the upper bounds of the function $\mu_\delta\left(\mathbf{G}_{\mathbf{w_P}\rightarrow\mathbf{z_P}}(j\omega_\mu,t)\right)$ across a dense grid of frequencies ω_μ and for several different values of the scheduling parameter $t \in [0,600]$. The function $\mu_\delta(\mathbf{G})$ represents the structured singular value [16] and provides very precise information about the magnitude of uncertainty which is needed to destabilize the loop at any frequency [15]. This function is equal to 0 if there is no uncertainty $\boldsymbol{\Delta}$ making $\mathbf{I}-\mathbf{G}\boldsymbol{\Delta}$ singular and it is equal to $\mu_\delta(\mathbf{G}) = 1/\underset{\boldsymbol{\Delta}}{min}\{\bar{\sigma}(\boldsymbol{\Delta}), \det(\mathbf{I}-\mathbf{G}\boldsymbol{\Delta}) = 0\}$ otherwise. In this context, μ_δ gives a measure of the smallest structured uncertainty $\mathbf{\Delta}$ that causes closed-loop instability for any frequency $\omega_\mu \in \mathbb{R}$. However, due to its non-convex character, μ_δ can be difficult to compute exactly. For that reason, some very efficient algorithms [17] have been developed in order to estimate the bounds of μ_δ. Fig. 10 depicts the upper bounds of μ_δ for different subsets of uncertainty. These bounds are computed for different values of t in Fig. 10a and across multiple frequencies in Fig. 10b, with $\mathbf{\Delta}_{sloshc} = \mathrm{diag}\left(\mathbf{\Delta}_{m_1}, \dots, \mathbf{\Delta}_{m_6}\right)$ and $\mathbf{\Delta}_{slosht} = \mathrm{diag}\left(\mathbf{\Delta}_{m_7}, \dots, \mathbf{\Delta}_{m_{12}}\right)$. The peak of μ_δ occurs for $t = 0$ s and for frequencies around $\omega_{\mathcal{S}_{7-12}}$. However, even when combining all the uncertainty subsets, μ_δ remains below 0.22 and therefore the loop can tolerate an increase in the uncertainty $\mathbf{\Delta_P}$ of 354% while maintaining stability.

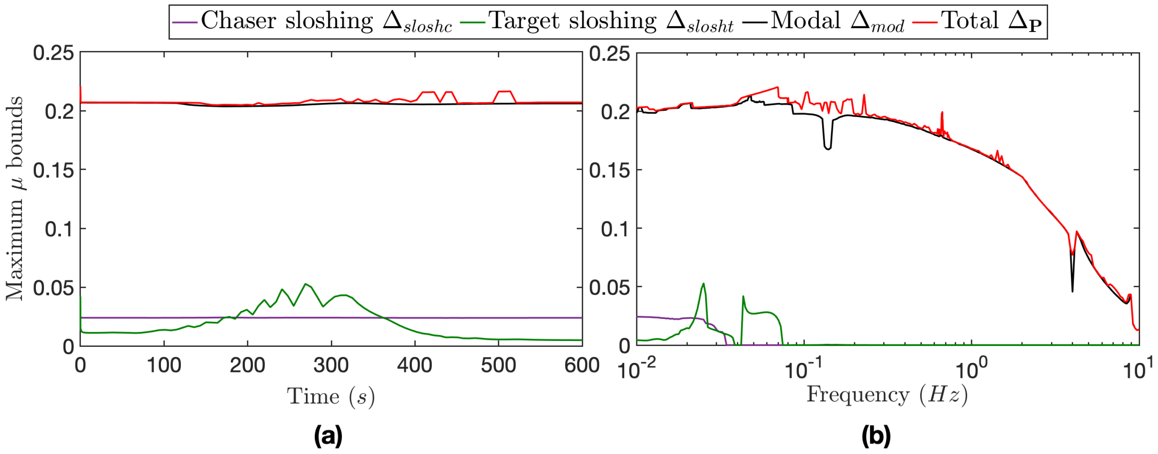

Figure 10: Robust stability plots with respect to different subsets of uncertainty: (a) upper bounds for different values of t. (b) upper bounds across a dense grid of frequencies.

The impact of all the subsets of uncertainty was also assessed for different performance indicators using structured singular value computations. Fig. 11 illustrates the upper bounds on the peak gain for different performance signals across all frequencies ω_μ and scheduling parameter values t. The first performance transfers $\mathbf{d}_u \to \mathbf{e}_p$ can be observed in Fig. 11a, which correspond to the absolute pointing error tracking channels. In this case, the highest peak and worst-case scenario happens for frequencies around 0.02 Hz and $t = 10.4$ s due to interactions between the controller and the plant dynamics. The worst-case gains of the performance channels $\mathbf{d}_u \to \mathbf{e}_u$ corresponding to the maximum control effort are shown in Fig. 11b. Similarly to the behavior depicted in Fig. 11a, it can be observed that the channels maintain values close to nominal ones even in the presence of significant model uncertainty. Afterwards, there is a visible roll-off, which is caused by $\mathbf{F}_{ro}(s)$. It can also be seen in Figs. 11a and 11b that the upper bounds stay below both requirements, which are given by $0.0284\,\mathrm{rad}$ and $1.2\,\mathrm{N\,m}$, respectively.

Ultimately, Fig. 12 shows the singular values of $\mathbf{G}(s,t)$ for the channel $\mathbf{d}_u\{3\} \to \mathbf{e}_p\{3\}$ as a function of the scheduling parameter t, together with the gains of the worst-case scenario found in Fig. 11 for the channels $\mathbf{d}_u \to \mathbf{e}_p$ when considering $\mathbf{\Delta_P}$ (worst-case configuration of $\mathbf{\Delta_P}$ found for frequencies around 0.02 Hz and $t = 10.4$ s, as stated before). The gains are always below 0 dB, meaning that the hard constraint imposed in Eq. (11) is complied with.

This study is merely a glimpse of the potential offered by the TITOP multi-body approach. Constructing a model of any multibody flexible structure in LFR form through this approach allows for the identification of worst-case scenarios without resorting to time-consuming Monte-Carlo methods that are typically employed in the industry. In contrast to the standard point-wise Monte-Carlo analysis, the approach proposed in this paper ensures complete coverage of the uncertainty space by means of a worst-case analysis.

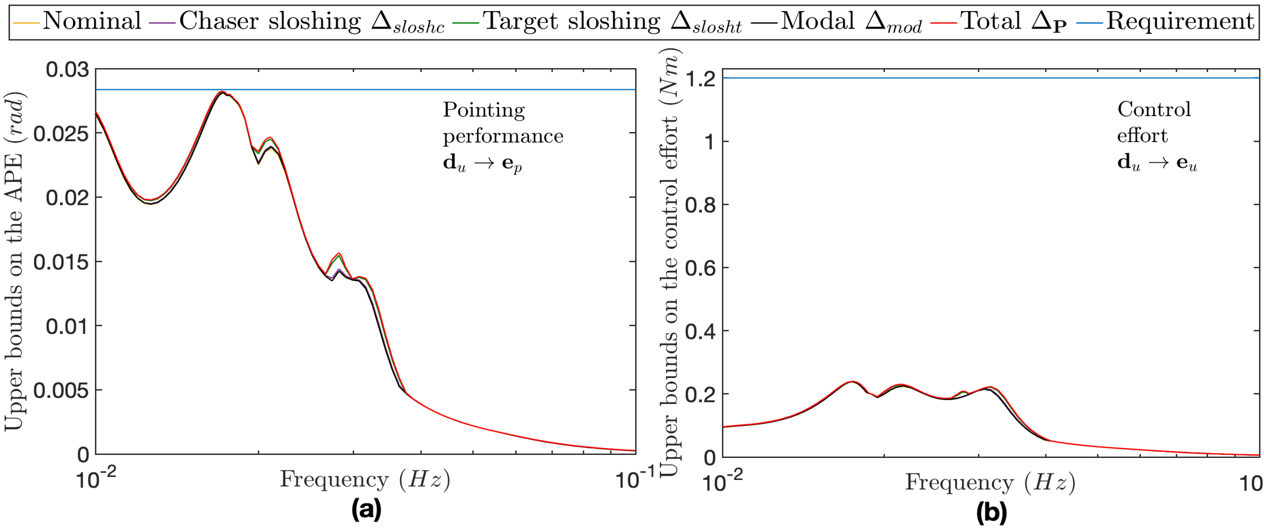

(a) **(b)**

Figure 11: Upper bounds on the gains of different performance channels with respect to different uncertainty sets: (a) the absolute pointing error tracking channels $\mathbf{d}_u \rightarrow \mathbf{e}_p$. (b) the control effort channels $\mathbf{d}_u \rightarrow \mathbf{e}_u$.

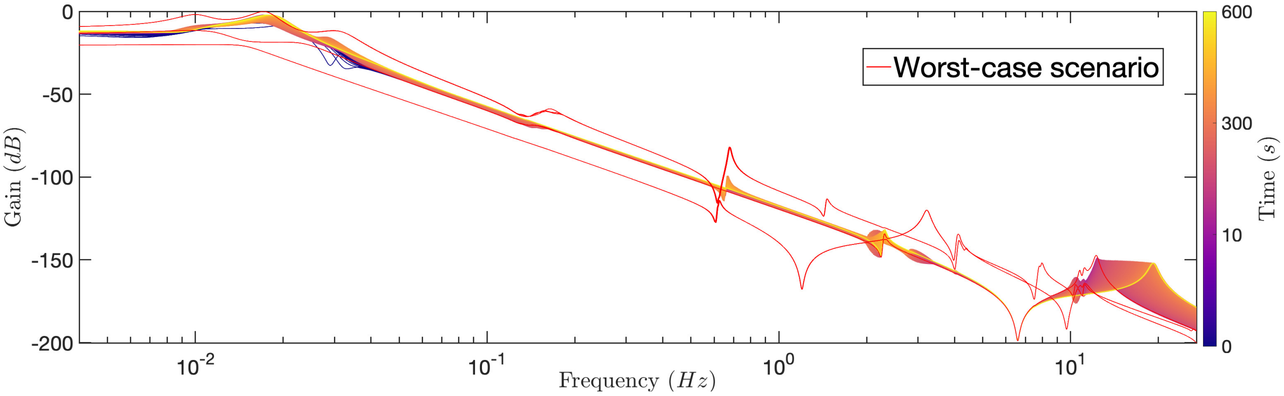

Figure 12: Singular values of the channel $\mathbf{d}_u\{3\} \rightarrow \mathbf{e}_p\{3\}$ as a function of the scheduled parameter t and gains of the worst-case scenario found for the channels $\mathbf{d}_u \rightarrow \mathbf{e}_p$.

5 CONCLUSION

This paper proposes a comprehensive modeling and control design methodology intended for on-orbit servicing scenarios. The presented framework exhibits the intricate nature of OOS missions, which are often marked by complex and challenging interactions between coupled flexible spacecraft, robotic arms and sloshing dynamics. To address this complexity, the proposed methodology aims to develop a compact system representation that incorporates all relevant elements, with a view to achieving a coherent and effective design model. The paper also offers a detailed overview of the controller synthesis procedure, highlighting how to account for the different requirements and performance limits. An essential aspect of this methodology is the posterior robust performance and stability assessment, which serves as a necessary step towards ensuring the safety and reliability of the proposed control law. The process of evaluating performance can provide useful insights into system design and control, enabling the adjustment of structural designs or even the optimization of mechanical parameters. Furthermore, the methodology's ability to perform Validation and Verification cycles in a preliminary phase without high computational burden simulations is a crucial advantage. Ultimately, it should be noted that the methodology described in this paper is based on the assumption that the system experiences minor deflections and maintains mostly linear dynamics. This assumption is applicable to a broad range of space-related applications, as spacecraft typically avoid large deflections and nonlinearities in structural dynamics by design.

Table 1: Chaser and target spacecraft mechanical data.

	Parameter	**Description**	**Value and Uncertainty**
Chaser's rigid hub $\mathcal{B}_1$	$\overrightarrow{G_1P_{1,2}}$	distance vector between G_1 and $P_{1,2}$ written in $\mathcal{R}_{\mathcal{B}_1}$	$[0,\ \pm 0.4365,\ 0]$ m
	$\overrightarrow{G_1J_0}$	distance vector between G_1 and J_0 written in $\mathcal{R}_{\mathcal{B}_1}$	$[0.6508,\ 0,\ -0.4020]$ m
	$m_{\mathcal{B}_1}$	mass of $\mathcal{B}_1$	188.5 kg
	$\begin{bmatrix} J_{xx}^{\mathcal{B}_1} & J_{xy}^{\mathcal{B}_1} & J_{xz}^{\mathcal{B}_1} \\ & J_{yy}^{\mathcal{B}_1} & J_{yz}^{\mathcal{B}_1} \\ & & J_{zz}^{\mathcal{B}_1} \end{bmatrix}$	inertia of $\mathcal{B}_1$ at G_1 written in $\mathcal{R}_{\mathcal{B}_1}$	$\begin{bmatrix} 41.98 & 3.84 & 0 \\ & 43.89 & 0 \\ & & 42.64 \end{bmatrix}$ kg m^2
Chaser's solar arrays $\mathcal{A}_{1,2}$	$\overrightarrow{P_{1,2}S_{1,2}}$	distance vector between $P_{1,2}$ and $S_{1,2}$ written in $\mathcal{R}_{\mathcal{A}_{1,2}}$	$[0,\ 1.0934,\ 0.0014]$ m
	$m_{\mathcal{A}_{1,2}}$	mass of $\mathcal{A}_{1,2}$	88.93 kg
	$\begin{bmatrix} J_{xx}^{\mathcal{A}_{1,2}} & J_{xy}^{\mathcal{A}_{1,2}} & J_{xz}^{\mathcal{A}_{1,2}} \\ & J_{yy}^{\mathcal{A}_{1,2}} & J_{yz}^{\mathcal{A}_{1,2}} \\ & & J_{zz}^{\mathcal{A}_{1,2}} \end{bmatrix}$	inertia of $\mathcal{A}_{1,2}$ at $S_{1,2}$ written in $\mathcal{R}_{\mathcal{A}_{1,2}}$	$\begin{bmatrix} 33.0918 & 0 & 0 \\ & 7.3819 & -0.0002 \\ & & 40.4578 \end{bmatrix}$ kg m^2
	$[\omega_{1_{\mathcal{A}_{1,2}}}, \omega_{2_{\mathcal{A}_{1,2}}}, \omega_{3_{\mathcal{A}_{1,2}}}, \omega_{4_{\mathcal{A}_{1,2}}}, \omega_{5_{\mathcal{A}_{1,2}}}, \omega_{6_{\mathcal{A}_{1,2}}}]$	flexible modes' frequencies	$[1.2850 \pm 20\%,\ 6.5896,\ 7.5231,\ 9.6937,\ 26.1311,\ 28.2408]$ Hz
	$[\xi_{1_{\mathcal{A}_{1,2}}}, \xi_{2_{\mathcal{A}_{1,2}}}, \xi_{3_{\mathcal{A}_{1,2}}}, \xi_{4_{\mathcal{A}_{1,2}}}, \xi_{5_{\mathcal{A}_{1,2}}}, \xi_{6_{\mathcal{A}_{1,2}}}]$	flexible modes' damping	$[0.01, 0.01, 0.01, 0.01, 0.01, 0.01]$
	$\mathbf{L}_{P_{1,2}}^{\mathcal{A}_{1,2}}$	modal participation factors	$\begin{bmatrix} -0.0007 & -0.0078 & 7.8872 & 11.7690 & 0.0005 & 0.0010 \\ -7.9401 & 0 & 0.0007 & -0.0008 & 0.1089 & 12.1014 \\ -0.3604 & 0 & 0.0006 & 0.0017 & -2.6631 & 0.5399 \\ 0.0019 & -0.0066 & 3.9818 & 0.9098 & -0.0007 & -0.0033 \\ 0.0272 & 0.0003 & -0.0145 & -0.0019 & 0.4907 & -0.0221 \\ -0.0010 & 0.0357 & -2.2185 & -0.2320 & -0.0029 & 0.0012 \end{bmatrix}$
Chaser's fuel particles $\mathcal{S}_{1-6}$	$r_{G_1C_{1-6}}$	distance between G_1 and C_{1-6}	0.2 m
	$m_{\mathcal{S}_{1-6}}$	mass of $\mathcal{S}_{1-6}$	$10.8291 \pm 20\%$ kg
	$k_{\mathcal{S}_{1-6}}$	springs stiffnesses	8 N m^{-1}
	$c_{\mathcal{S}_{1-6}}$	springs damping coefficients	0.8367 N s m^{-1}
Target's rigid hub $\mathcal{B}_2$	$\overrightarrow{G_2P_{3,4}}$	distance vector between G_2 and $P_{3,4}$ written in $\mathcal{R}_{\mathcal{B}_2}$	$[0,\ \pm 0.3395,\ 0]$ m
	$m_{\mathcal{B}_2}$	mass of $\mathcal{B}_2$	24.96kg
	$\begin{bmatrix} J_{xx}^{\mathcal{B}_2} & J_{xy}^{\mathcal{B}_2} & J_{xz}^{\mathcal{B}_2} \\ & J_{yy}^{\mathcal{B}_2} & J_{yz}^{\mathcal{B}_2} \\ & & J_{zz}^{\mathcal{B}_2} \end{bmatrix}$	inertia of $\mathcal{B}_2$ at G_2 written in $\mathcal{R}_{\mathcal{B}_2}$	$\begin{bmatrix} 2.684 & 0.058 & 0.054 \\ & 2.012 & -0.104 \\ & & 2.32 \end{bmatrix}$ kg m^2
Target's solar arrays $\mathcal{A}_{3,4}$	$\overrightarrow{P_{3,4}S_{3,4}}$	distance vector between $P_{3,4}$ and $S_{3,4}$ written in $\mathcal{R}_{\mathcal{A}_{3,4}}$	$[0,\ 0.7446,\ 0]$ m
	$m_{\mathcal{A}_{3,4}}$	mass of $\mathcal{A}_{3,4}$	11.3497 kg
	$\begin{bmatrix} J_{xx}^{\mathcal{A}_{3,4}} & J_{xy}^{\mathcal{A}_{3,4}} & J_{xz}^{\mathcal{A}_{3,4}} \\ & J_{yy}^{\mathcal{A}_{3,4}} & J_{yz}^{\mathcal{A}_{3,4}} \\ & & J_{zz}^{\mathcal{A}_{3,4}} \end{bmatrix}$	inertia of $\mathcal{A}_{3,4}$ at $S_{3,4}$ written in $\mathcal{R}_{\mathcal{A}_{3,4}}$	$\begin{bmatrix} 1.9566 & 0 & 0 \\ & 0.3404 & 0 \\ & & 2.2968 \end{bmatrix}$ kg m^2
	$[\omega_{1_{\mathcal{A}_{3,4}}}, \omega_{2_{\mathcal{A}_{3,4}}}, \omega_{3_{\mathcal{A}_{3,4}}}, \omega_{4_{\mathcal{A}_{3,4}}}, \omega_{5_{\mathcal{A}_{3,4}}}, \omega_{6_{\mathcal{A}_{3,4}}}]$	flexible modes' frequencies	$[0.6493 \pm 20\%,\ 2.2480,\ 3.9870,\ 4.3455,\ 10.9601,\ 18.2744]$ Hz
	$[\xi_{1_{\mathcal{A}_{3,4}}}, \xi_{2_{\mathcal{A}_{3,4}}}, \xi_{3_{\mathcal{A}_{3,4}}}, \xi_{4_{\mathcal{A}_{3,4}}}, \xi_{5_{\mathcal{A}_{3,4}}}, \xi_{6_{\mathcal{A}_{3,4}}}]$	flexible modes' damping	$[0.01, 0.01, 0.01, 0.01, 0.01, 0.01]$
	$\mathbf{L}_{P_{3,4}}^{\mathcal{A}_{3,4}}$	modal participation factors	$\begin{bmatrix} 0.0003 & 0 & -2.7332 & -2.8462 & 0.0001 & -0.0003 \\ 2.8655 & 0 & 0 & 0.0002 & -0.0025 & -2.9305 \\ -0.0002 & 0 & -1.5206 & -0.3709 & 0.0022 & 0.0003 \\ -0.0119 & 0 & -0.0058 & -0.0017 & -0.5800 & 0.0123 \\ 0 & 0 & 0.8207 & 0.0958 & 0.0002 & -0.0001 \\ 0.0008 & 0.0001 & -0.0007 & 0 & 0.0596 & -0.0009 \end{bmatrix}$
Target's fuel particles $\mathcal{S}_{7-12}$	$r_{G_2C_{7-12}}$	distance between G_2 and C_{7-12}	0.1 m
	$m_{\mathcal{S}_{7-12}}$	mass of $\mathcal{S}_{7-12}$	$2.1658 \pm 20\%$ kg
	$k_{\mathcal{S}_{7-12}}$	springs stiffnesses	2 N m^{-1}
	$c_{\mathcal{S}_{7-12}}$	springs damping coefficients	0.2510 N s m^{-1}

REFERENCES

[1] V. Dubanchet, S. Andiappane, P. L. Negro, D. Casu, A. Giovannini, G. Durand, and J. D'Amico, "Validation and demonstration of EROSS project: The european robotic orbital support services," in *IAC 2020*, 2020.

[2] Y. Liu, X. Chen, Y. Zhang, and C. Li, "Sample data game strategy for active rendezvous with disturbance rejection," *Aerospace Science and Technology*, vol. 121, p. 107358, 2022.

[3] J. D. Biggs and S. Brisotto, "Robust spacecraft rendezvous using a variable speed control moment gyro and thruster," *Aerospace Science and Technology*, vol. 112, p. 106644, 2021.

[4] D. Henry, J. Zenteno-Torres, J. Cieslak, A. Ferreira De Loza, and J. Dávila, “A 6-dof sliding mode fault tolerant control solution for in-orbit autonomous rendezvous,” *Aerospace Science and Technology*, vol. 118, p. 107050, 2021.

[5] S. Samsam and R. Chhabra, “Multi-impulse smooth trajectory design for long-range rendezvous with an orbiting target using multi-objective non-dominated sorting genetic algorithm,” *Aerospace Science and Technology*, vol. 120, p. 107285, 2022.

[6] Y. Chai, J. Luo, N. Han, and J. Sun, “Robust event-triggered game-based attitude control for on-orbit assembly,” *Aerospace Science and Technology*, vol. 103, p. 105894, 2020.

[7] R. Rodrigues, V. Preda, F. Sanfedino, and D. Alazard, “Modeling, robust control synthesis and worst-case analysis for an on-orbit servicing mission with large flexible spacecraft,” *Aerospace Science and Technology*, vol. 129, p. 107865, 2022.

[8] C. J. Allard, M. D. Ramos, H. Schaub, and S. Piggott, *Spacecraft Dynamics Integrating Hinged Solar Panels and Lumped-Mass Fuel Slosh Model*.

[9] J. A. Perez, D. Alazard, T. Loquen, C. Cumer, and C. Pittet, “Linear dynamic modeling of spacecraft with open-chain assembly of flexible bodies for acs/structure co-design,” in *Advances in Aerospace Guidance, Navigation and Control*, J. Bordeneuve-Guibé, A. Drouin, and C. Roos, Eds. Cham: Springer International Publishing, 2015, pp. 639–658.

[10] F. Sanfedino, D. Alazard, V. Pommier-Budinger, A. Falcoz, and F. Boquet, “Finite element based n-port model for preliminary design of multibody systems,” *Journal of Sound and Vibration*, vol. 415, pp. 128–146, 2018.

[11] F. Sanfedino, P. Valentin, and D. Oddenino, “Integrated modeling of microvibrations induced by solar array drive mechanism for worst-case end-to-end analysis and robust disturbance estimation,” *Mechanical Systems and Signal Processing*, vol. 163, p. 108168, 06 2021.

[12] D. Alazard and F. Sanfedino, “Satellite dynamics toolbox library (sdtlib) - user’s guide,” March 2021.

[13] N. Guy, D. Alazard, C. Cumer, and C. Charbonnel, “Dynamic modeling and analysis of spacecraft with variable tilt of flexible appendages,” *Journal of Dynamic Systems, Measurement, and Control*, vol. 136, no. 2, p. 0, Jan. 2014.

[14] P. Apkarian and D. Noll, “Nonsmooth $\mathcal{H}_\infty$ Synthesis,” *IEEE Transactions on Automatic Control*, vol. 51, no. 1, pp. 71–86, 2006.

[15] V. Preda, F. Sanfedino, S. Bennani, F. Boquet, and D. Alazard, “Robust and adaptable dynamic response reshaping of flexible structures,” *Journal of Sound and Vibration*, vol. 468, p. 115086, 2020.

[16] A. Packard and J. Doyle, “The complex structured singular value,” *Automatica*, vol. 29, no. 1, pp. 71–109, 1993.

[17] G. Balas, R. Chiang, A. Packard, and M. Safonov, “Robust control toolbox user’s guide,” *The Math Works, Inc., Tech. Rep*, 2007.